

Electrostatic polarity-regulated, vinylene-linked cationic covalent organic frameworks as an ionic sieve membrane for long-cyclable lithium-sulfur batteries

Linhai Sun^{a,1}, Zhongping Li^{b,1}, Lipeng Zhai^{a,*}, Hyunseok Moon^b, Cheng Song^c, Kyeong-Seok Oh^b, Xiangtao Kong^d, Diandian Han^a, Zhiqiang Zhu^a, Yang Wu^{c,*}, Sang-Young Lee^{b,*}, Liwei Mi^{a,*}

^a Henan Key Laboratory of Functional Salt Materials, Center for Advanced Materials Research, Zhongyuan University of Technology, Zhengzhou 450007, PR China

^b Department of Chemical and Biomolecular Engineering, Yonsei University, 50, Yonsei-ro, Seodaemun-gu, Seoul 03772, Republic of Korea

^c Department of Chemical Engineering, School of Environmental and Chemical Engineering, Shanghai University, Shanghai, 200444, PR China

^d Henan Key Laboratory of New Optoelectronic Functional Materials, College of Chemistry and Chemical Engineering, Anyang Normal University, Anyang 455000, PR China

ARTICLE INFO

Keywords:

Cationic covalent organic frameworks
Electrostatic polarity
Ionic sieve membrane
Dissociation of Li⁺
Lithium sulfur battery

ABSTRACT

Lithium-sulfur (Li-S) batteries have garnered attention as a promising alternative to commercial Li-ion batteries owing to their high theoretical energy density and the natural abundance of sulfur. However, the uncontrolled dendrite growth of Li metal anodes and shuttle effect of polysulfides have plagued their practical application. To address these issues, here, we present electrostatic polarity-regulated, vinylene-linked cationic covalent organic frameworks (COFs) as a class of ionic sieve membranes. The electrostatic polarity of the COFs was controlled by varying the counter anions adjacent to the cationic framework. The higher electrostatic polarity achieved with a bulkier anion, combined with the one-dimensional nanochannels of the COFs, suppressed polysulfide crossover, while facilitating Li⁺ conduction, demonstrating the viability of the ionic sieving effect of the membrane. Consequently, the Li-S cell fabricated with the COF-based ionic sieve membrane exhibited a low capacity degradation of 0.041 % per cycle over 1000 cycles at a fast current rate of 1 C.

1. Introduction

Benefiting from the high theoretical energy density (2600 Wh kg⁻¹) and natural abundance of sulfur, lithium-sulfur (Li-S) batteries have attracted considerable attention as a potential candidate for post-LIB energy storage devices [1–5]. However, some challenges hinder the practical application of Li-S batteries, such as the inhomogeneous deposition of Li, which results in unwanted dendrite growth from Li metal anodes and the formation of dead Li during cycling [6–9]. In addition, the continuous shuttle effect of the negatively charged lithium polysulfides (LiPS) between the sulfur cathode and Li anode results in a decline in the capacity and the structural deterioration of the electrode during cycling [10–13].

Many previous works have focused on the use of porous carbons or organic polymers as sulfur hosts to trap sulfur species through physical

and/or chemical interaction [14–17]. However, the inability of most of these approaches to resolve the trade-off between Li⁺ transport and the shuttle effect has limited their further application. Moreover, as both the Li dendrite growth and shuttle effect problems are closely related to the ion transport phenomena through separator membranes, they both can be addressed by developing advanced separator membranes [18–21]. Accordingly, various functional materials, such as metal oxides, metal-organic frameworks, nanostructured carbon, sulfides, and MXenes, have been investigated to modify separator membranes [22–26]. However, the incorporation of these functional materials results in the loss of ionic conductivity in the resulting separator membranes. Therefore, a new membrane design that can provide permselectivity (to facilitate the uniform Li⁺ migration while simultaneously suppressing the shuttle effect) is urgently required.

Covalent organic frameworks (COFs), which are characterized with

* Corresponding authors.

E-mail addresses: zhailp@zut.edu.cn (L. Zhai), yang.wu@shu.edu.cn (Y. Wu), syleek@yonsei.ac.kr (S.-Y. Lee), 6379@zut.edu.cn (L. Mi).

¹ These authors contributed equally

highly customizable structures and functionalities at the molecular level owing to their abundant building units and linkages, have emerged as a promising material in many fields, such as catalysis, gas storage, and energy storage [27–51]. Owing to their highly ordered one-dimensional (1D) pore channels and precisely tunable functionalities, COFs have been investigated as an attractive alternative to separator membranes. For example, Loh et al. recently constructed nanofluidic interface separator membranes for high-performance Li–S cells using fluorinated COFs [52]. Additionally, Wang et al. reported sulfonate-rich COF-modified separator membranes with strong electronegativity [53]. Further, Sun et al. fabricated lithiated COF nanosheets (Li-CON)-coated separator membranes [54]. These studies demonstrated that compared to neutral COFs, ionic COFs exhibit unique advantages for designing separator membranes owing to the surface charge-induced electrostatic ion screening and the corresponding electrostatic repulsion. However, ionic COFs with different electrostatic polarity have rarely been explored in separator membranes for Li–S cells.

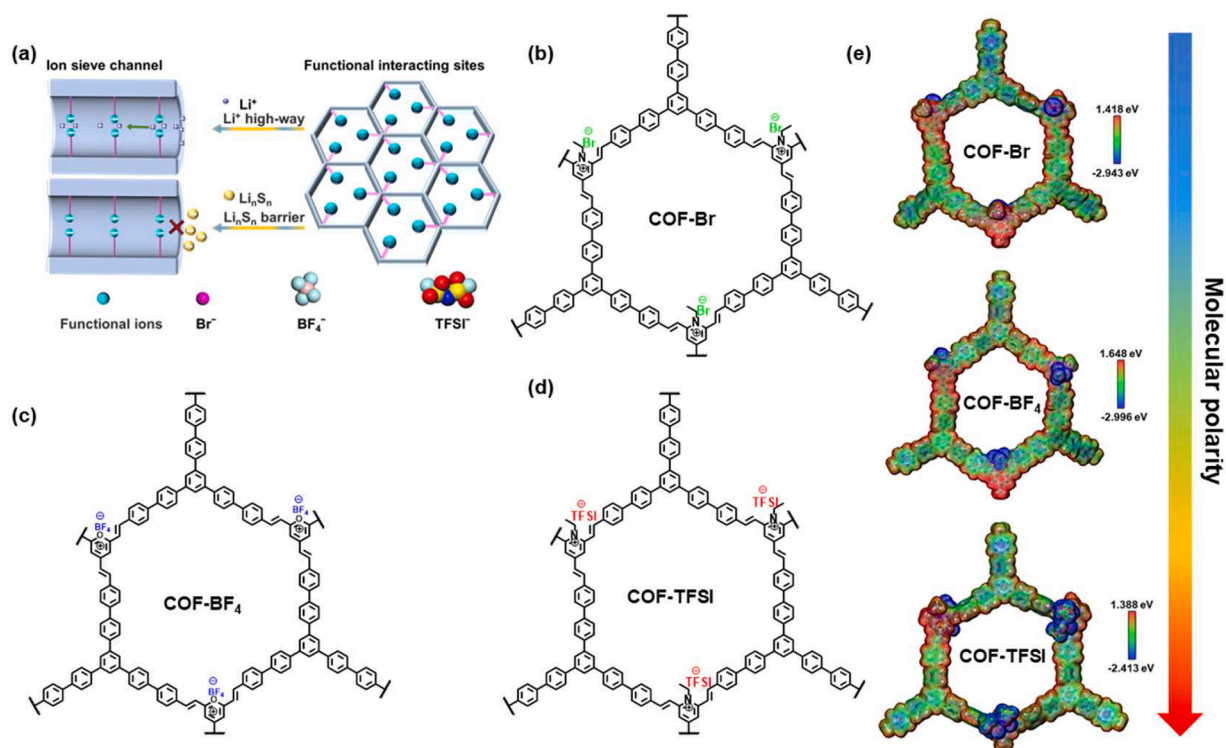
Here, we report electrostatic polarity-regulated, vinylene-linked cationic COFs as a class of ionic sieve membranes for long-cyclable Li–S cells. The electrostatic polarity of the COFs was controlled by varying the counter anions (bromide (Br^-), tetrafluoroborate (BF_4^-), bis(trifluoromethyl)sulfonyl)azanide (TFSI $^-$)) adjacent to the cationic framework (Scheme 1a). Notably, introduction of a high density of a bulkier anion (TFSI $^-$) into the 1D nanochannels of the COFs promoted the intermolecular interaction between the COFs and ionic species (Li^+ or LiPS), thereby suppressing the crossover of anionic LiPS, while simultaneously facilitating Li^+ conduction.

The COF-TFSI was applied as a coating layer to functionalize a commercial polyolefin separator. The resulting modified separator membrane (denoted as “COF-TFSI separator”) enabled stable Li plating/stripping cyclability (over 800 h at a fast current density of 5.0 mA cm^{-2} and a high capacity of 5.0 mAh cm^{-2}) in a Li||Li symmetric cell. In addition, a Li–S cell with the COF-TFSI separator exhibited long cycle retention (only 0.041 % capacity loss per cycle over 1000 cycles).

Particularly, the cell achieved a high areal capacity of $4.23 \text{ mA h cm}^{-2}$ after 100 cycles with a high sulfur loading of 8.81 mg cm^{-2} and lean electrolyte of $5 \mu\text{L mg}^{-1}$, outperforming previously reported COFs-based Li–S cells.

2. Results and discussion

We synthesized a set of vinylene-linked COFs with similar skeleton but different ionic pore channels (Br^- , BF_4^- , and TFSI $^-$; denoted as COF-Br, COF- BF_4 , and COF-TFSI, respectively. Scheme 1b–d). The electrostatic potential of these COFs is shown in Scheme 1e and the corresponding electrostatic polarities of the COFs was in the following order: COF-Br < COF- BF_4 < COF-TFSI (Table S1). The increased electrostatic polarity of COF-Br, COF- BF_4 , and COF-TFSI could improve the interaction between COFs and Li ions, resulting in the accelerated migration of Li ions. Besides, the anions in the systems could be repelled by the increased electrostatic polarity of these COFs. Therefore, the increased electrostatic polarity of COFs exhibited positive influence on the ion-sieving effect and electrochemical performance of resulting Li–S cells. In this study, COF-Br and COF- BF_4 were synthesized using 1,3,5-tris-(4'-formyl-biphenyl-4-yl)benzene (TFBB) and N-ethyl-2,4,6-trimethylpyridinium bromide (ETMP-Br) or 2,4,6-trimethyl-pyrylium tetrafluoroborate (TMP- BF_4) via the Knoevenagel condensation (Fig. S1). The chemical structure of these COFs was investigated using Fourier transform infrared (FT-IR) spectroscopy. Two new peaks emerged at approximately 1634 and 967 cm^{-1} in the FT-IR spectra of these samples, and were attributed to the stretching and bending vibrations of carbon–carbon double bond, indicating the successful formation of vinylene linkage in COF-Br and COF- BF_4 (Fig. S2). Additionally, the peaks corresponding to $\text{C}=\text{O}$ at 1701 cm^{-1} in the FT-IR spectra of the corresponding aldehyde monomer in the two COFs disappeared, suggesting the high polymerization degree of the samples. The stepwise weight loss of COF-Br and COF- BF_4 was observed in their thermogravimetric analysis (TGA) curves, particularly in the low temperature region. This result



Scheme 1. (a) Schematic illustration of the ion sieve channels in the cationic COFs and its contribution to the facile Li^+ transport and electrostatic repulsion with the anionic LiPS. Chemical structure of the cationic COFs: (b) COF-Br, (c) COF- BF_4 , and (d) COF-TFSI. (e) Electrostatic potential and molecular polarity of the COF-Br, COF- BF_4 , and COF-TFSI.

might be attributed to the degradation of the ionic groups in the pore channels of the COFs (Fig. S3). Next, field emission scanning electron microscopy (FE-SEM) revealed that COF-Br and COF-BF₄ exhibited sphere-like morphology (Fig. S4), and the corresponding energy dispersive spectroscopy (EDS) profiles showed that the composition elements of the two COFs were distributed uniformly over the frameworks (Figs. S5 and S6).

The crystalline structures of the COFs were investigated using powder X-ray diffraction (PXRD) measurement. Four peaks were observed in the PXRD pattern of COF-Br at 3.90, 6.87, 17.88, and 25.9°, which were assigned to the 100, 110, 011, and 001 facets, respectively (Fig. 1a, red curve). Additionally, five characteristic PXRD peaks were observed in the PXRD pattern of COF-BF₄ at 4.12, 7.13, 12.62, 15.25, and 24.32°, which corresponded to the 100, 110, 300, 040, and 001 facets, respectively (Fig. 1b, red curve). The corresponding theoretical structures of the COFs were investigated using density function tight binding (DFTB⁺) method. The PXRD curves (Fig. 1, purple circles) simulated from Pawley refinements of these two COFs could reproduce the experimental PXRD profiles, evidenced by the negligible differences in the satisfactory residues (5.82 % of R_{wp} , 4.37 % of R_p for COF-Br and 6.47 % of R_{wp} , 5.12 % of R_p for COF-BF₄; Fig. 1, black curves). Meanwhile, the PXRD curves (Fig. 1, yellow curves) calculated from the AA stacking mode were well matched with the experimentally observed PXRD patterns of both COFs. In contrast, there were notable differences between the PXRD calculated

from the AB stacking mode and the experimental PXRD profiles (Fig. 1, purple curves).

The permanent porosity of COF-Br and COF-BF₄ was investigated using N₂ sorption at 77 K. The two COFs exhibited typical type-I isotherms, indicating that they exhibited microporous structures (Fig. S7). The pore size distribution analysis was calculated using the nonlocal density functional theory (NLDFT) cylindrical pore model. The pore sizes of COF-Br and COF-BF₄ were determined to be 1.57 and 1.54 nm, respectively (Fig. S8), which were consistent with their theoretical pore sizes calculated from their frameworks.

The COF-TFSI was prepared by replacing Br⁻ with TFSI⁻ in aqueous lithium bis(trifluoromethane)sulfonimide (LiTFSI) solution to through an ion-exchange strategy (Fig. S9). The FE-SEM image of the sample after the ion exchange suggested that there was no notable morphological change (Fig. S10). Additionally, the TGA curve of COF-TFSI displayed similar degradation behavior with that of COF-Br, and the notable degradation observed at approximately 400 °C might to be attributed to the degradation of the TFSI group (Fig. S11). The chemical structure information of the COF-TFSI was examined using FT-IR and XPS profiles. Four characteristic peaks (1050, 1126, 1179, and 1343 cm⁻¹) corresponding to the TFSI group were observed in the FT-IR spectrum of COF-TFSI between 1000 and 1400 cm⁻¹ and the peaks for vinyne linkage were retained, indicating that Br⁻ was successfully replaced by TFSI⁻ and the skeleton was retained after ion exchange

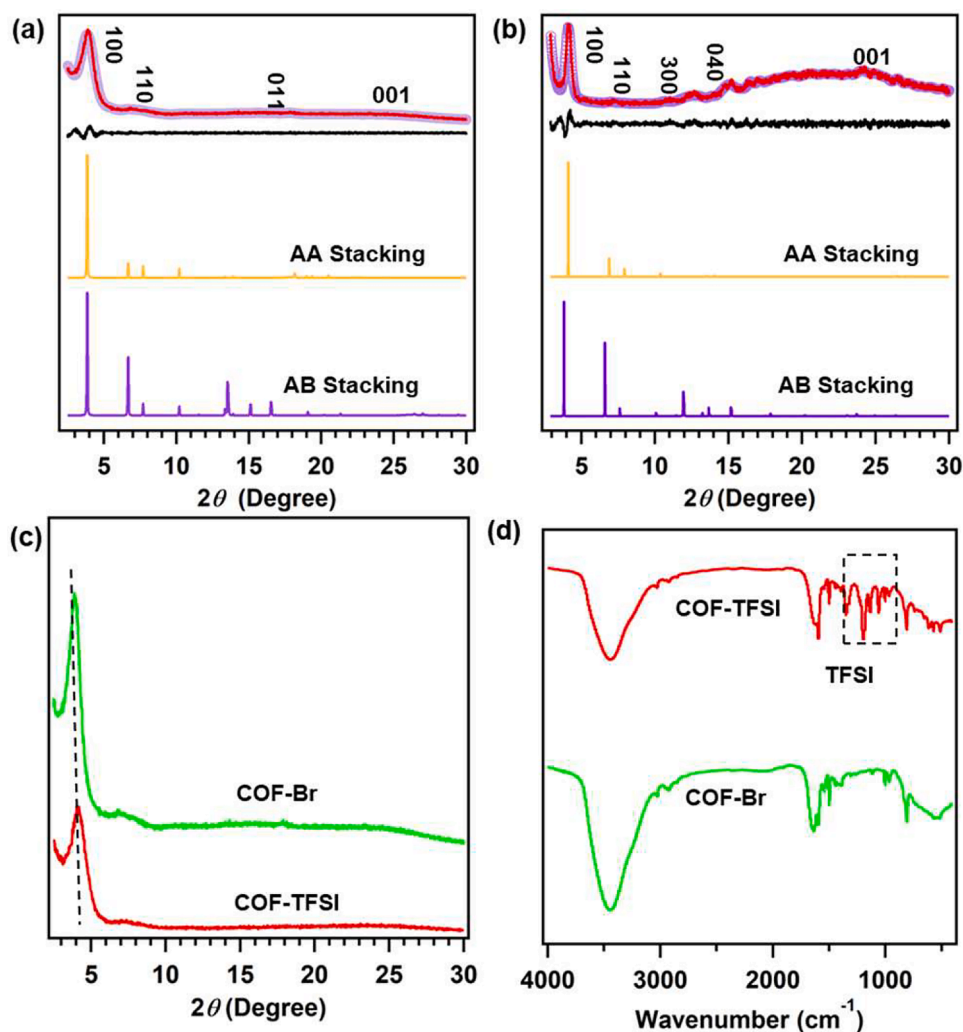


Fig. 1. PXRD patterns of (a) COF-Br and (b) COF-BF₄: the experimental XRD patterns (red curves), the refined patterns (purple circles), the difference between the observed and refined profiles (black curves), simulated XRD curves from the AA stacking (yellow curves) and AB stacking (purple curves) modes. (c) PXRD patterns of COF-Br and COF-TFSI. (d) FT-IR spectra of COF-Br and COF-TFSI.

process (Fig. 1d). The peaks corresponding to Br^- in the XPS profiles of COF-Br (Fig. S12) and COF-TFSI (Fig. S13) at 71.1 and 68.6 eV (Br 3d) almost disappeared, and new peaks emerged at approximately 687.5 eV and 686 (F1s) and 170.17 and 168.9 eV (S 2p), which were attributed to TFSI⁻, indicating the complete exchange of all the Br^- in COF-Br by TFSI⁻. After the ion exchange, COF-TFSI displayed similar peaks with COF-Br (Fig. 1c). The peak corresponding to the 100 facet shifted from 3.90 (COF-Br) to 4.11° in the spectra of COF-TFSI owing to the larger size of TFSI⁻ group in COF-TFSI compared with Br^- in COF-Br. The pore size of COF-TFSI was 1.52 nm, respectively (Fig. S14). The decreased BET surface area and pore size of COF-TFSI might attributed to be the larger size of TFSI ion compared to that of Br^- .

Subsequently, the as-synthesized COF samples were uniformly pelt on the surface of a commercial separator (Celgard 2500) with a thickness of 10 μm and mass loading amount of approximately 0.43 mg cm^{-2} (Figs. S15–17). The corresponding wettability of different separators toward the electrolyte was investigated using contact angle (CA) measurements (Fig. 2a). The CA of COFs toward the electrolyte was in the following order: COF-TFSI (5.9°) < COF- BF_4 (7.9°) < COF-Br (11.2°). These values are significantly smaller than that of the Celgard separator (43.4°). This indicates that the coating of ionic COFs on the surface of Celgard is an effective method for improving electrolyte adsorption, thus promoting ion migration. The ion transport behaviour of these modified membranes was investigated using electrochemical impedance spectroscopy (EIS), with a focus on ionic conductivity and ionic mobility (Fig. 2b). The ionic conductivities of COF-TFSI, COF- BF_4 , COF-Br and Celgard were 1.63, 1.41, 1.31, and 0.72 mS cm^{-1} , respectively (Fig. 2c). The enhanced ionic conductivity of COF-TFSI might be attributed to the synergistic effect of the enhanced wettability and electrostatic interaction between the COFs coating and electrolyte. The Li^+ transference numbers (t_{Li^+}) of Celgard, COF-Br, COF- BF_4 , and COF-TFSI were estimated to be 0.50, 0.73, 0.76, and 0.84, respectively (Fig. S18). Consequently, the Li^+ ion conductivity (= ionic conductivity $\times t_{\text{Li}^+}$) of Celgard, COF-Br, COF- BF_4 , and COF-TFSI were calculated to be 0.36, 0.96, 1.07, and 1.37 mS cm^{-1} , respectively. This result demonstrated that the integration of COFs on the Celgard as a coating layer is

beneficial for enhancing the Li^+ migration. Besides, the anionic conductivity of Celgard, COF-Br, COF- BF_4 , and COF-TFSI were calculated to be 0.36, 0.35, 0.34, and 0.26, respectively, indicating that the transport of anions in these systems can be suppressed after the introduction of COF coating layers on the Celgard. These results exhibited that the Li^+ migration can be enhanced while suppressing the anion (Br^- , BF_4^- , and TFSI⁻) conduction, demonstrating the ion-sieving effect of the COFs on different ions. These results exhibited the enhanced ionic migration and repressed anion (Br^- , BF_4^- , TFSI⁻) transport. The ion-selective transport behavior was dominated by the corresponding anions the negatively charged pore channels, which promoted the migration of cations and blocks the transport of anions, particularly for TFSI⁻-functionalized COF.

Li symmetric batteries were prepared using various COFs modified separators to investigate the reaction kinetics of Li anode using Tafel plots. The batteries with different COFs-modified separators (COF-TFSI > COF- BF_4 > COF-Br) exhibited the enhanced exchange current density compared to the battery with Celgard, indicating accelerated Li^+ migration via the integration of ionic groups in the pore channels, particularly for TFSI (Fig. 2d). Moreover, the influence of ionic COFs modified separators on the performance of Li metal was further characterized using Li|Li symmetric cells. The rate performance of the batteries with COFs-modified separators exhibited narrower voltage hysteresis than that of the cell with pristine Celgard separator and the smallest value was achieved for the cell with COF-TFSI separator (Fig. 2e). The cell with the Celgard separator exhibited the largest voltage hysteresis (≥ 400 mV) at all the current densities, whereas the cell with COF-TFSI achieved a stable and the smallest voltage hysteresis under the same condition. Additionally, the long-term cycling measurement revealed that the battery with COF-TFSI exhibited the lowest and stable polarization behavior (16 mV) at a current density of 1.0 mA cm^{-2} and a capacity of 1.0 mAh cm^{-2} (Fig. 2f). Meanwhile, at a larger current density of 5.0 mA cm^{-2} and a capacity of 5.0 mAh cm^{-2} , the cell with COF-TFSI still exhibited the lowest and stable polarization behavior (33 mV) (Fig. 2g). These results demonstrated that the introduction of ionic COFs coating on the surface of Celgard (particularly COF-TFSI) significantly constrained the growth of Li dendrites. To further

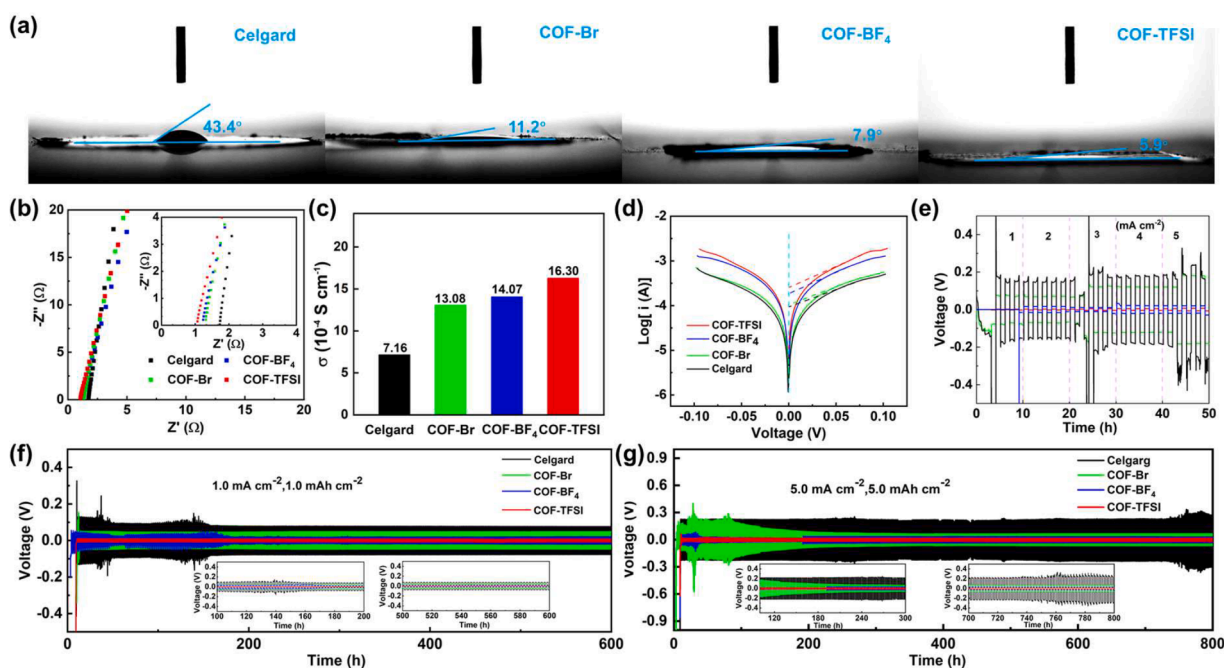


Fig. 2. (a) Contact angles of the liquid electrolyte on: Celgard, COF-Br@Celgard, COF- BF_4 @Celgard, and COF-TFSI@Celgard separator. (b) EIS plots of the various separators. (c) Ionic conductivity of the various separators. (d) Tafel plots of the Li|Li symmetrical cells with the various separators at a scan rate of 0.2 mV s^{-1} between -0.1 and 0.1 V. (e) Rate performance of the Li|Li symmetric cells with the various separators. (f, g) Voltage profiles of the Li|Li symmetric cells with the various separators.

elucidate this superior cyclability of the COF-TFSI, we examined the surface of the cycled Li metal anodes (Fig. S19). The results demonstrated that the cell with COF-TFSI exhibited a uniform and smooth Li surface compared to the other separators. This result indicates that the COF-TFSI separator was beneficial for uniform and facile Li^+ flux, which results in stable Li plating/stripping on the Li metal anode.

The LiPS shuttle effect severely restricts the commercialization of sulfur cathodes. In this study, the H-type electrolytic cell was utilized to conduct permeation experiments to directly visualize the effect of COFs on the prevention of the shuttle effect (Fig. S20). To this end, the left border of a H-type electrolytic battery was filled with LiPS (10 mM Li_2S_8) solution and the right side was filled with the clear electrolyte (DOL/DME, 1:1 by volume). The various separators were placed between the two electrolytic sides. For the Celgard separator, after 0.5 h, LiPS migration was observed, and the color gradually became deeper with time. In contrast, for the COF-Br and COF- BF_4 separators, the hindrance of LiPS migration was observed and the color of the right-side electrolyte only became deeper after 3 and 6 h, respectively. When COF-TFSI separator was employed, the right-side electrolyte maintained a clear color with no notable color change even after 12 h. These results confirmed the ability of the COF-TFSI coating layer to inhibit the LiPS shuttle.

The corresponding electrochemical performance of the Li-S cells was tested by combining sulfur cathode ($\sim 1.2 \text{ mg cm}^{-2}$), COFs-coated separators, and Li anode. The electrochemical impedance spectroscopy (EIS) plots (Fig. S21) revealed that the charge transfer resistance (R_{ct}) of the pristine cells was in the order of COF-TFSI (11.85Ω) < COF- BF_4

(15.84Ω) < COF-Br (16.25Ω), which were all lower than that of the battery with the Celgard separator (18.58Ω). This can be attributed to the enhanced wettability of the COFs-modified separators toward the electrolyte, which improved the ion migration kinetics, particularly for COF-TFSI. Two typical reduction peaks were observed in the cyclic voltammetry (CV) curves (Fig. S22) of the Li-S cells with the COFs-modified separators at ~ 2.25 and ~ 1.95 V at scanning rates from 0.1 to 0.5 mV s^{-1} . These peaks suggested the occurrence of the multistep reduction of S_8 to the long-chain soluble LiPS (Li_2S_x , $4 \leq x \leq 8$) and then to $\text{Li}_2\text{S}_2/\text{Li}_2\text{S}$, respectively. The oxidation peak at ~ 2.45 V during the charging process can be attributed to the complicated process conversion of Li_2S to S_8 . The diffusion characteristics of Li_2S_n could be evaluated indirectly based on that of Li^+ , which were analyzed from the CV curves at different scanning rates. According to the Randles-Sevcik equation, the slope of the fitted line corresponds to the Li^+ diffusion rate, which can positively reflect the mobility of Li^+ within the electrode (Fig. S23). The slope value of the battery with COF-TFSI was higher than those of the batteries with COF- BF_4 , COF-Br, and Celgard, which further indicated the positive influence of COF-TFSI on the Li^+ diffusion rate. The polarization voltage was investigated using the third galvanostatic charge-discharge curves at 0.2 C, and the cell with COF-TFSI separator exhibited the smallest polarization (170 mV) compared to the cells with COF- BF_4 (176 mV), COF-Br (179 mV), and the pristine Celgard (304 mV) separators, demonstrating the superior kinetics of redox conversion reactions (Fig. 3a).

The cyclic performance of the Li-S cells with various separators was investigated at a rate of 0.2 C (Fig. 3b). The battery with COF-TFSI

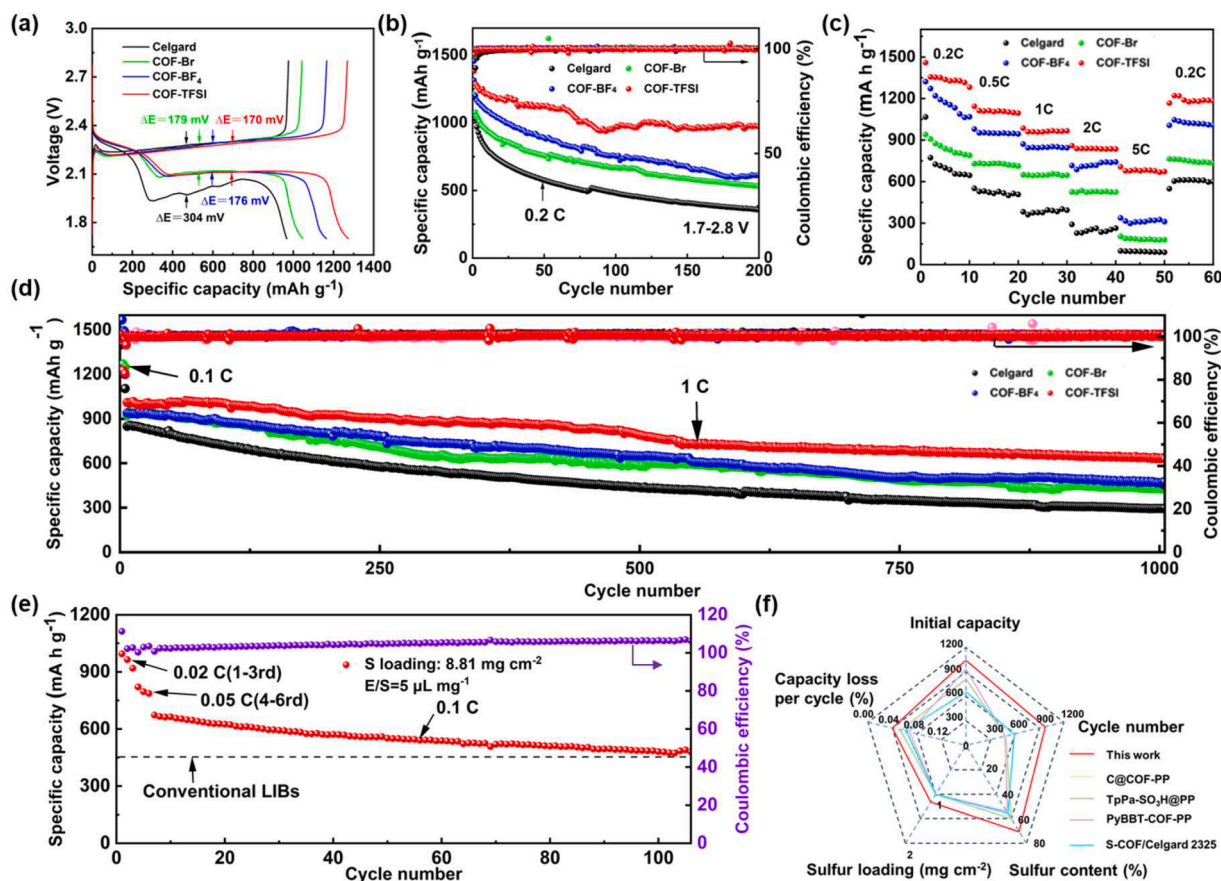


Fig. 3. Cell performance of the Li-S cells with the various separators. (a) Charge-discharge voltage profiles at charge/discharge current density of 0.2 C / 0.2 C. (b) Capacity retention performance at charge/discharge current density of 0.2 C / 0.2 C. (c) Discharge rate capability at a fixed charge current density of 0.2–5 C. (d) Cycling performance at charge/discharge current density of 1.0 C / 1.0 C. (e) Cycling performance of the Li-S cell with the COF-TFSI separator with a high sulfur loading of 8.81 mg cm^{-2} at charge/discharge current density of 0.1 C / 0.1 C. (f) Cell performance comparison between this study and those of previously reported Li-S cells containing functional separators.

exhibited an initial discharge capacity of 1381 mAh g^{-1} , which was significantly higher than that of the batteries with COF-BF₄ (1313 mAh g^{-1}), COF-Br (1211 mAh g^{-1}), and Celgard (1188 mAh g^{-1}). The COF-TFSI battery experienced a slow decay rate and a high Coulomb efficiency (CE) in the subsequent cycles, and achieved the highest discharge capacity of 973 mAh g^{-1} at the 200th cycle. After the 200th cycles, the weekly attenuation rate of COF-TFSI was 0.15% , which was significantly lower than those of COF-BF₄@Celgard (0.26%), COF-Br (0.28%), and that of Celgard (0.35%). The rate performances of the COFs batteries were evaluated at various current densities ($0.2, 0.5, 1, 2$, and 5 C ; Fig. 3c). The COF-TFSI-modified battery delivered capacities of $1460, 1144, 987, 859$, and 707 mAh g^{-1} at current densities of $0.2, 0.5, 1, 2$, and 5 C , respectively, which were higher than those of the batteries based on COF-BF₄, COF-Br, and Celgard at different current densities. The COFs-modified batteries recovered their initial capacity after the current density was returned back to 0.2 C , indicating stable electrochemistry of sulfur and rate performance. Even at a high rate of 5.0 C , the COF-TFSI battery exhibited a low polarization voltage of 0.43 V (Fig. S24). In contrast, at the same rate, the charge-discharge curves of COF-BF₄, COF-Br, and Celgard batteries exhibited larger polarization voltages. Moreover, the charge and discharge curves of COF-TFSI, COF-BF₄, COF-Br, and Celgard batteries at $0.2, 0.5, 1, 2$, and 5 C

demonstrated that the battery with COF-TFSI exhibited the smallest polarization voltage (Fig. S25).

To investigate the corresponding long-term cyclic performance, the Li-S batteries with COFs were cycled at a large current density of 1 C ($\sim 3.5 \text{ mA cm}^{-2}$; Fig. 3d). The battery with COF-TFSI displayed an initial specific capacity of 1066 mAh g^{-1} and the capacity was maintained at 630 mAh g^{-1} after 1000 cycles, with only a 0.041% capacity loss per cycle over 1000 cycles. The battery with COF-BF₄ exhibited a capacity of 1044 mAh g^{-1} at the first cycle at 1 C and 516 mAh g^{-1} after 1000 cycles, with a weekly capacity decay rate of 0.055% . The capacity of the battery with COF-Br was 957 mAh g^{-1} at the first cycle and 429.8 mAh g^{-1} after 1000 cycles at 1 C , with the capacity decay rate of 0.057% . The battery with Celgard demonstrated the lowest capacity of 863 mAh g^{-1} at the first cycle and 294 mAh g^{-1} after 1000 cycles at 1 C , with the largest capacity decay rate of 0.066% .

The use of the ionic COFs-modified separators significantly improved the cycling performance of the battery, indicating a significant inhibition in the shuttle of LiPS in the COFs modified batteries, particularly for the COF-TFSI. Additionally, the improved ion transport ability in the COF-TFSI battery was beneficial to the high-rate performance. Furthermore, the corresponding electrochemical performances of batteries with high sulfur loading and electrolyte deficiency was

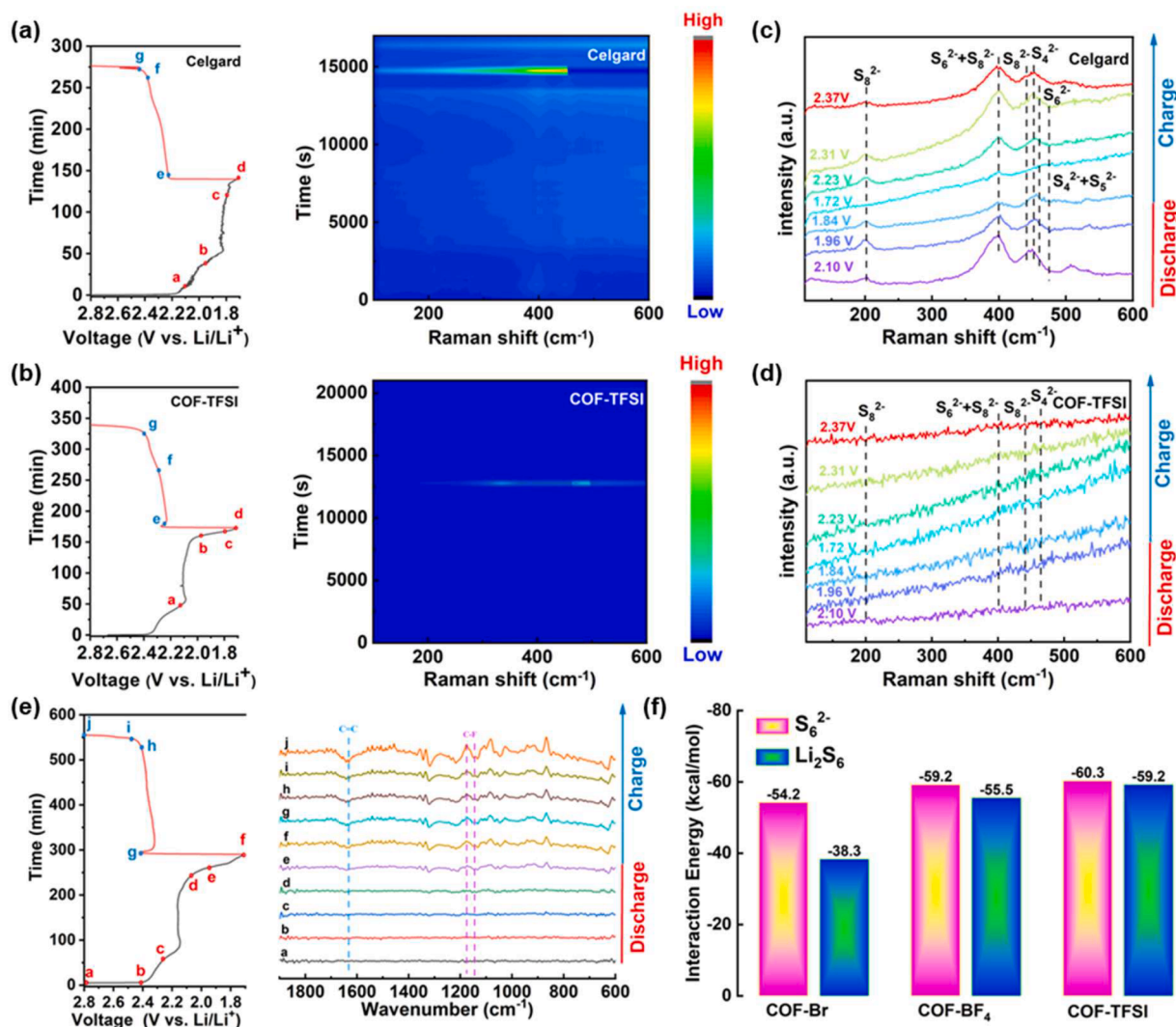


Fig. 4. *In situ* time-resolved Raman spectra obtained during the discharge reaction with (a) Celgard and (b) COF-TFSI separators. Selected Raman spectroscopy of the Li-S cells with (c) Celgard and (d) COF-TFSI separators. (e) Voltage profile of the Li-S cell with the COF-TFSI separator at charge/discharge current density of $0.2 \text{ C} / 0.2 \text{ C}$, and the points labeled with a–j indicate the different charge/discharge states that were assigned the FT-IR spectra. (f) Interaction between sulfur species (S_6^{2-} and Li_2S_6) and various COFs.

investigated to evaluate the potential practical application of the Li–S cell with the COF-TFSI separator. To this end, S/BP2000 cathodes with 71.3 % sulfur content (Fig. S26) were fabricated and employed to investigate the electrochemical properties under a high sulfur loading (8.81 mg cm^{-2}) and lean electrolytes ($5 \text{ } \mu\text{L mg}^{-1}$). Under a high sulfur loading of 8.81 mg cm^{-2} and after six cycles of activation, the specific discharge capacities of the battery with COF-TFSI after the first cycle was 673 mAh g^{-1} at a current rate of 0.1 C (Fig. 3e). After 100 cycles, the capacity retention rate was 71.3 %. The batteries with COF-TFSI separator (Fig. 3f and Table S2) displayed superior performance in terms of capacity retention at high rates, cycle stability, and areal capacity compared to previously reported Li–S batteries with functional layers and traditional modified separators.

Next, *in-situ* Raman spectroscopy was conducted to reveal the LiPS shuttle effect on the Li metal anode in real-time and investigate the role of ionic vinylene-linked COFs in inhibiting the LiPS shuttle. The time-resolved Raman contour maps and selected Raman signals of the cells with COF-TFSI separator and Celgard at different discharge/charge states (Fig. 4a–d) were compared. For the cell with the Celgard separator, the S_8^{2-} signals at 203, 400, and 445 cm^{-1} was observed at the initial discharge stage (2.10 V), suggesting the formation of the long-chain soluble Li_2S_8 and its shuttling across the separator. During the discharge process, the intensity of the S_8^{2-} signals slightly decreased and the peaks at approximately 451, 475 and 460 cm^{-1} , corresponding to the characteristics S_4^{2-} , S_5^{2-} , and S_6^{2-} , respectively, appeared simultaneously. Moreover, during the charge process, the prominent characteristic peaks of S_4^{2-} , S_5^{2-} , S_6^{2-} , and S_8^{2-} could be observed, indicating the occurrence of the LiPS shuttle and the irreversible loss of sulfur species. However, the cell with the COF-TFSI separator exhibited weak Raman peaks of LiPS during the discharge and charge processes, suggesting that the polysulfides migration was effectively repelled. Moreover, the characteristic FT-IR peaks of the C–F bond (Fig. 4e) were distinctly observed. Herein, the PVDF contents of these systems were identical. Thus, the intensity difference of FT-IR peaks for C–F bond could be ascribed to the strong interaction between COF-TFSI and Li^+ , indicating the strong interaction between COF-TFSI and Li^+ .

Additionally, the elemental composition of the surface of the Li anode of the as-prepared batteries after 200 cycles was analyzed using XPS. All the batteries with the COFs-modified separators were measured after the charging process. Four characteristic peaks were observed in the S 2p spectra at binding energies of 161.9, 163.1, 167.2, and 169.0 eV, in which the peak at 161.9 was attributed to $\text{Li}_2\text{S}/\text{Li}_2\text{S}_2$ (Fig. S27). Compared to those of the other batteries, the Li anode of the cell with the COF-TFSI separator exhibited a lower intensity of the $\text{Li}_2\text{S}/\text{Li}_2\text{S}_2$ peak, indicating the suppressed irreversible deposition of $\text{Li}_2\text{S}/\text{Li}_2\text{S}_2$ on the surface of Li anode. The cycled separators were immersed in DME solvent (Fig. S28). After being soaked for 1 h, the Celgard separator showed an obvious yellow color in the DME solvent, while the COFs separator showed a slightly light-yellow color in the DME solvent, especially for the COF-TFSI separator. These results indicated that the very limited amount of polysulfides could be adsorbed on the surface of COF-TFSI separator.

In addition, the XPS analysis of the disassembled cells revealed the detailed information of the absorbed polysulfides: COF-Br (Fig. S29), COF-BF₄ (Fig. S30), and COF-TFSI (Fig. S31) separators. Four characteristic peaks with the binding energies of 161.9, 163.1, 167.2 and 169.0 eV were observed in the S 2p spectra for these cycled COFs separators, in which the peak at 161.9 eV was attributed to $\text{Li}_2\text{S}/\text{Li}_2\text{S}_2$. The results suggested that the lowest intensity of $\text{Li}_2\text{S}/\text{Li}_2\text{S}_2$ was found for the COF-TFSI separator, indicating that the COF-TFSI separator exhibited lowest polysulfide absorption ability and the strongest inhibition of polysulfides absorption.

Further, the interaction energy density of COFs toward LiPS was investigated using density functional theory (DFT) calculations. Here, S_6^{2-} and Li_2S_6 were selected as representative LiPS examples to calculate the corresponding interaction with various COFs. The interaction energy

between S_6^{2-} and COFs exhibited a negative energy value, which confirmed the electrostatic repulsion between the LiPS and anions in the COFs pore channels (Fig. 4f). The energy values of these COFs toward S_6^{2-} was in the following order: COF-Br ($-54.2 \text{ kcal mol}^{-1}$) < COF-BF₄ ($-59.2 \text{ kcal mol}^{-1}$) < COF-TFSI ($-60.3 \text{ kcal mol}^{-1}$), indicating that COF-TFSI exhibited the largest repulsion ability towards S_6^{2-} , which is consistent with the electrochemical performance results of the Li–S cells. Moreover, the calculated results of the interaction energy between COFs and Li_2S_6 suggested that the LiPSs could be repulsed by the ionic COFs. The binding energies between COFs and LiPSs increased in the order of COF-Br to COF-BF₄ to COF-TFSI, with COF-TFSI exhibiting the largest binding energy ($-59.2 \text{ kcal mol}^{-1}$). These results suggested that LiPS could be effectively repelled across the pore channels owing to the electrostatic interaction between the ionic groups and LiPSs, which is consistent with the experimental results.

3. Conclusions

In this study, we presented electrostatic polarity-regulated, vinylene-linked cationic COFs as an ionic sieve membrane strategy to address the trade-off issue between Li^+ migration and the shuttle effect. Among the various counter anions examined herein, TFSI[−] effectively interacted with Li^+ or LiPS owing to the enhanced electrostatic polarity. Consequently, facile and uniform Li^+ conduction was achieved, leading to stable Li plating/stripping cyclability. Additionally, the enriched anionic environment in the 1D nanochannels of the COF-TFSI suppressed the shuttle effect of anionic LiPS. Consequently, the Li–S cells with the COF-TFSI separator exhibited improved rate capability and cycling stability (only a 0.041 % capacity loss per cycle over 1000 cycles). The COF-TFSI separator enabled the stable operation of Li–S cells under constrained cell conditions (high sulfur loading of 8.81 mg cm^{-2} and lean electrolyte of $5 \text{ } \mu\text{L mg}^{-1}$), highlighting its potential contribution to the development of practical Li–S cells. This electrostatic polarity-regulated cationic COF provides a new insight into the design of ionic sieve membranes and holds promise as a platform technology for next-generation batteries suffering from the conflicting ion transport phenomena.

Supporting Information is available from the online version or from the author.

CRedit authorship contribution statement

Lin Hai Sun: Writing – review & editing, Writing – original draft, Software, Data curation, Conceptualization. **Zhongping Li:** Writing – review & editing, Writing – original draft, Supervision, Software, Data curation, Conceptualization. **Lipeng Zhai:** Writing – review & editing, Writing – original draft, Supervision, Resources, Funding acquisition, Data curation, Conceptualization. **Hyunseok Moon:** Writing – review & editing, Writing – original draft, Data curation, Conceptualization. **Cheng Song:** Writing – review & editing, Writing – original draft, Data curation, Conceptualization. **Kyeong-Seok Oh:** Writing – review & editing, Writing – original draft, Data curation, Conceptualization. **Xiangtao Kong:** Writing – review & editing, Writing – original draft, Data curation. **Diandian Han:** Writing – review & editing, Writing – original draft, Data curation. **Zhiqiang Zhu:** Writing – review & editing, Writing – original draft, Data curation. **Yang Wu:** Writing – review & editing, Writing – original draft, Data curation. **Sang-Young Lee:** Writing – review & editing, Writing – original draft, Supervision, Data curation, Conceptualization. **Liwei Mi:** Writing – review & editing, Writing – original draft, Conceptualization.

Declaration of competing interest

The authors declare that they have no known competing financial interests or personal relationships that could have appeared to influence the work reported in this paper.

Data availability

Data will be made available on request.

Acknowledgements

This work was supported from the National Natural Science Foundation of China (52103277) and the Program for Science & Technology Innovation Talents in Universities of Henan Province (23HASTIT015). This work was also supported by National Research Foundation of Korea (NRF) funded by the Korean Government (MSIT) (No. RS-2023-00261543, 2022M3J1A1085397 and 2021M3H4A1A02099355).

Supplementary materials

Supplementary material associated with this article can be found, in the online version, at [doi:10.1016/j.ensm.2024.103222](https://doi.org/10.1016/j.ensm.2024.103222).

References

- Q. Fan, Y. Si, F. Zhu, W. Guo, Y. Fu, Activation of bulk Li_2S as cathode material for lithium-sulfur batteries through organochalcogenide-based redox mediation chemistry, *Angew. Chem. Int. Ed.* 62 (2023) e202306705, <https://doi.org/10.1002/anie.202306705>.
- P. Bruce, S. Freunberger, L. Hardwick, J.M. Tarascon, Li-O_2 and Li-S batteries with high energy storage, *Nat. Mater.* 11 (2012) 19–29, <https://doi.org/10.1038/nmat3191>.
- C. Cui, C. Yang, N. Eidson, J. Chen, F. Han, L. Chen, C. Luo, P.F. Wang, X. Fan, C. Wang, Highly reversible, dendrite-free lithium metal anode enabled by a lithium-fluoride-enriched interphase, *Adv. Mater.* 32 (2020) 1906427, <https://doi.org/10.1002/adma.201906427>.
- A. Manthiram, Y. Fu, S.H. Chung, C. Zu, Y.S. Su, Rechargeable lithium-sulfur batteries, *Chem. Rev.* 114 (2014) 11751–11787, <https://doi.org/10.1021/cr500062v>.
- H. Zhang, X. Judez, A. Santiago, M. Martínez-Ibañez, M. Muñoz-Márquez, J. Carrasco, C. Li, G. Eshetu, M. Armand, Fluorine-free noble salt anion for high-performance all-solid-state lithium-sulfur batteries, *Adv. Energy Mater.* 9 (2019) 1900763, <https://doi.org/10.1002/aenm.201900763>.
- H. Chen, A. Pei, D. Lin, J. Xie, A. Yang, J. Xu, K. Lin, J. Wang, H. Wang, F. Shi, D. Boyle, Y. Cui, Uniform high ionic conducting lithium sulfide protection layer for stable lithium metal anode, *Adv. Energy Mater.* 9 (2019) 1900858, <https://doi.org/10.1002/aenm.201900858>.
- Z.J. Zheng, H. Ye, Z.P. Guo, Recent progress on pristine metal/covalent-organic frameworks and their composites for lithium-sulfur batteries, *Energy Environ. Sci.* 14 (2021) 1835–1853, <https://doi.org/10.1039/D0EE03181J>.
- M.H. Ryou, D. Lee, J.N. Lee, Y. Lee, J.K. Park, J. Choi, Excellent cycle life of lithium-metal anodes in lithium-ion batteries with mussel-inspired polydopamine-coated separators, *Adv. Energy Mater.* 2 (2012) 645–650, <https://doi.org/10.1002/aenm.201100687>.
- C.Z. Zhao, P.Y. Chen, R. Zhang, X. Chen, B.Q. Li, X.Q. Zhang, X.B. Cheng, Q. Zhang, An ion redistributor for dendrite-free lithium metal anodes, *Sci. Adv.* 4 (2018) eaat3446, <https://doi.org/10.1126/sciadv.aat3446>.
- H. Dai, K. Xi, X. Liu, C. Lai, S. Zhang, Cationic surfactant-based electrolyte additives for uniform lithium deposition via lithiophobic repulsion mechanisms, *J. Am. Chem. Soc.* 140 (2018) 17515–17521, <https://doi.org/10.1021/jacs.8b08963>.
- Y. Yao, H. Wang, H. Yang, S. Zeng, R. Xu, F. Liu, P. Shi, Y. Feng, K. Wang, W. Yang, X. Wu, W. Luo, Y. Yu, A dual-functional conductive framework embedded with TiN-VN heterostructures for highly efficient polysulfide and lithium regulation toward stable Li-S full batteries, *Adv. Mater.* 32 (2020) 1905658, <https://doi.org/10.1002/adma.201905658>.
- R. Yan, B. Mishra, M. Traxler, J. Roeser, N. Chaoui, B. Kumbhakar, J. Schmidt, S. Li, A. Thomas, P. Pachfule, Thiazole-Linked covalent organic framework for lithium-sulphur batteries, *Angew. Chem. Int. Ed.* 62 (2023) e202302276, <https://doi.org/10.1002/anie.202302276>.
- M. Zhao, B.Q. Li, H.J. Peng, H. Yuan, J.Y. Wei, J.Q. Huang, Lithium-Sulfur batteries under lean electrolyte conditions: challenges and opportunities, *Angew. Chem. Int. Ed.* 59 (2020) 12636–12652, <https://doi.org/10.1002/anie.201909339>.
- S. Shen, X. Xia, Y. Zhong, S. Deng, D. Xie, B. Liu, Y. Zhang, G. Pan, X. Wang, J. Tu, Implanting niobium carbide into trichoderma spore carbon: a new advanced host for sulfur cathodes, *Adv. Mater.* 31 (2019) 1900009, <https://doi.org/10.1002/adma.201900009>.
- J. He, G. Hartmann, M. Lee, G. Hwang, Y. Chen, A. Manthiram, Freestanding 1T MoS_2 /Graphene heterostructures as a highly efficient electrocatalyst for lithium polysulfides in Li-S batteries, *Energy Environ. Sci.* 12 (2019) 344–350, <https://doi.org/10.1002/adma.201900009>.
- T. Lei, W. Chen, W. Lv, J. Huang, J. Zhu, J. Chu, C. Yan, C. Wu, Y. Yan, W. He, J. Xiong, Y. Li, C. Yan, X. Duan, Inhibiting polysulfide shuttling with a graphene composite separator for highly robust lithium-sulfur batteries, *Joule* 2 (2018) 2091–2104, <https://doi.org/10.1016/j.joule.2018.07.022>.
- X.J. Hong, C.L. Song, Y. Yang, H.C. Tan, G.H. Li, Y.P. Cai, H. Wang, Cerium based metal-organic frameworks as an efficient separator coating catalyzing the conversion of polysulfides for high performance lithium-sulfur batteries, *ACS. Nano* 13 (2019) 1923–1931, <https://doi.org/10.1021/acsnano.8b08155>.
- X. Li, X. Sun, Interface design and development of coating materials in lithium-sulfur batteries, *Adv. Funct. Mater.* 28 (2018) 1801323, <https://doi.org/10.1002/adfm.201801323>.
- Y. Li, W. Wang, X. Liu, E. Mao, M. Wang, G. Li, L. Fu, Z. Li, A. Eng, Z. Seh, Y. Sun, Engineering stable electrode-separator interfaces with ultrathin conductive polymer layer for high-energy-density Li-S batteries, *Energy Storage Mater.* 23 (2019) 261–268, <https://doi.org/10.1016/j.ensm.2019.05.005>.
- J. Xu, W. Tang, C. Yang, I. Manke, N. Chen, F. Lai, T. Xu, S. An, H. Liu, Z. Zhang, Y. Cao, N. Wang, S. Zhao, D. Niu, R. Chen, A highly conductive COF@CNT electrocatalyst boosting polysulfide conversion for Li-S chemistry, *ACS. Energy Lett.* 6 (2021) 3053–3062, <https://doi.org/10.1021/acsenergylett.1c00943>.
- S. Bai, X. Liu, K. Zhu, S. Wu, H. Zhou, Metal-Organic framework-based separator for lithium-sulfur batteries, *Nat. Energy* 1 (2016) 16094, <https://doi.org/10.1038/energy.2016.94>.
- Y. Zang, F. Pei, J. Huang, Z. Fu, G. Xu, X. Fang, Large-Area preparation of crack-free crystalline microporous conductive membrane to upgrade high energy lithium-sulfur batteries, *Adv. Energy Mater.* 8 (2018) 1802052, <https://doi.org/10.1002/aenm.201802052>.
- Y. Luo, N. Luo, W. Kong, H. Wu, K. Wang, S. Fan, W. Duan, J. Wang, Multifunctional interlayer based on molybdenum diphosphide catalyst and carbon nanotube film for lithium-sulfur batteries, *Small* 14 (2018) 1702853, <https://doi.org/10.1002/smll.201702853>.
- L. Jiao, C. Zhang, C. Geng, S. Wu, H. Li, W. Lv, Y. Tao, Z. Chen, G. Zhou, J. Li, G. W. Ling, Y. Wan, Q.H. Yang, Capture and catalytic conversion of polysulfides by In situ built TiO_2 -MXene heterostructures for lithium-sulfur batteries, *Adv. Energy Mater.* 9 (2019) 1900219, <https://doi.org/10.1002/aenm.201900219>.
- H. Chen, Y. Xiao, C. Chen, J. Yang, C. Gao, Y. Chen, J. Wu, Y. Shen, W. Zhang, S. Li, F. Huo, B. Zheng, Conductive MOF-Modified separator for mitigating the shuttle effect of lithium-sulfur battery through a filtration method, *ACS Appl. Mater. Interfaces* 11 (2019) 11459–11465, <https://doi.org/10.1021/acsaami.8b22564>.
- F. Wu, S. Zhao, L. Chen, Y. Lu, Y. Jia, L. Bao, J. Wang, S. Chen, R. Chen, Metal-Organic frameworks composites threaded on the CNT knitted separator for suppressing the shuttle effect of lithium sulfur batteries, *Energy Storage Mater.* 14 (2018) 383–391, <https://doi.org/10.1016/j.ensm.2018.06.009>.
- L. Deng, Z. Ding, X. Ye, D. Jiang, Covalent organic frameworks: chemistry of pore interface and wall surface perturbation and impact on functions, *Acc. Mater. Res.* 3 (2022) 879–893, <https://doi.org/10.1021/accountsmr.2c00108>.
- J. Ding, X. Guan, J. Lv, X. Chen, Y. Zhang, H. Li, D. Zhang, S. Qiu, H.L. Jiang, Q. Fang, Three-dimensional covalent organic frameworks with ultra-large pores for highly efficient photocatalysis, *J. Am. Chem. Soc.* 145 (2023) 3248–3254, <https://doi.org/10.1021/jacs.2c13817>.
- M. Feng, Z. Niu, C. Xing, Y. Jin, X. Feng, Y. Zhang, B. Wang, Covalent organic framework based crosslinked porous microcapsules for enzymatic catalysis, *Angew. Chem. Int. Ed.* 62 (2023) e202306621, <https://doi.org/10.1002/anie.202306621>.
- Z. Mu, Y. Zhu, Y. Zhang, A. Dong, C. Xing, Z. Niu, B. Wang, X. Feng, Hierarchical microtubular covalent organic frameworks achieved by COF-to-COF transformation, *Angew. Chem. Int. Ed.* 135 (2023) e202300373, <https://doi.org/10.1002/ange.202300373>.
- S. Jia, L. Hao, Y. Liu, E. Lin, W. Liu, Y. Yang, Y. Tian, Y. Peng, P. Cheng, Y. Chen, Z. Zhang, Freestanding hydrophilic/hydrophobic janus covalent organic framework membranes for highly efficient solar steam generation, *ACS Mater. Lett.* 5 (2023) 458–465, <https://doi.org/10.1021/acsmaterlett.2c01056>.
- Y. Yang, C. Zhang, G. Zhao, Q. An, Z.Y. Mei, Y. Sun, Q. Xu, X. Wang, H. Guo, Regulating the electron structure of covalent organic frameworks by strong electron-withdrawing nitro to construct specific Li^+ oriented channel, *Adv. Energy Mater.* 13 (2023) 2300725, <https://doi.org/10.1002/aenm.202300725>.
- D. Chen, W. Chen, Y. Wu, L. Wang, X. Wu, H. Xu, L. Chen, Covalent organic frameworks containing dual O_2 reduction centers for overall photosynthetic hydrogen peroxide production, *Angew. Chem. Int. Ed.* 135 (2023) e202217479, <https://doi.org/10.1002/ange.202217479>.
- B. Shi, X. Pang, S. Li, H. Wu, J. Shen, X. Wang, C. Fan, L. Cao, T. Zhu, M. Qiu, Z. Yin, Y. Kong, Y. Liu, M. Zhang, Y. Liu, F. Pan, Z. Jiang, Short hydrogen-bond network confined on COF surfaces enables ultrahigh proton conductivity, *Nat. Commun.* 13 (2022) 6666, <https://doi.org/10.1038/s41467-022-33868-8>.
- Y. Qian, Y. Han, X. Zhang, G. Yang, G. Zhang, H. Jiang, Computation-based regulation of excitonic effects in donor-acceptor covalent organic frameworks for enhanced photocatalysis, *Nat. Commun.* 14 (2023) 3083, <https://doi.org/10.1038/s41467-023-38884-w>.
- Z.B. Zhou, P.J. Tian, J. Yao, Y. Lu, Q.Y. Qi, X. Zhao, Toward azo-linked covalent organic frameworks by developing linkage chemistry via linker exchange, *Nat. Commun.* 13 (2022) 2180, <https://doi.org/10.1038/s41467-022-29814-3>.
- X. Xu, X. Wu, K. Xu, H. Xu, H. Chen, N. Huang, Pore partition in two-dimensional covalent organic frameworks, *Nat. Commun.* 14 (2023) 3360, <https://doi.org/10.1038/s41467-023-39126-9>.
- T. Zhou, L. Wang, X. Huang, H.Z. Junruangsri, R. Wang, Q. Song, Q. Yang, W. Li, C. Wang, H. Xu, J. Guo, PEG-Stabilized coaxial stacking of two-dimensional covalent organic frameworks for enhanced photocatalytic hydrogen evolution, *Nat. Commun.* 12 (2021) 3934, <https://doi.org/10.1038/s41467-021-24179-5>.

- [39] Z. Li, T. Deng, S. Ma, Z. Zhang, G. Wu, J. Wang, Q. Li, H. Xia, S.W. Yang, X. Liu, Three-component donor- π -acceptor covalent-organic frameworks for boosting photocatalytic hydrogen evolution, *J. Am. Chem. Soc.* 145 (2023) 8364–8374, <https://doi.org/10.1021/jacs.2c11893>.
- [40] Y. Su, Y. Wan, H. Xu, K.I. Otake, X. Tang, L. Huang, S. Kitagawa, C. Gu, Crystalline and stable benzofuran-linked covalent organic frameworks from irreversible cascade reactions, *J. Am. Chem. Soc.* 142 (2020) 13316–13321, <https://doi.org/10.1021/jacs.0c05970>.
- [41] Q. Wu, R.K. Xie, M.J. Mao, G.L. Chai, J.D. Yi, S.S. Zhao, Y.B. Huang, R. Cao, Integration of strong electron transporter tetrathiafulvalene into metalloporphyrin-based covalent organic framework for highly efficient electroreduction of CO₂, *ACS. Energy Lett.* 5 (2020) 1005–1012, <https://doi.org/10.1021/acseenergylett.9b02756>.
- [42] K. Zhang, X. Li, L. Ma, F. Chen, Z. Chen, Y. Yuan, Y. Zhao, J. Yang, J. Liu, K. Xie, Fluorinated covalent organic framework-based nanofluidic interface for robust lithium–sulfur batteries, *ACS. Nano* 17 (2023) 2901–2911, <https://doi.org/10.1021/acsnano.2c11300>.
- [43] F. Meng, S. Bi, Z. Sun, B. Jiang, D. Wu, J.S. Chen, F. Zhang, Synthesis of ionic vinylene-linked covalent organic frameworks through quaternization-activated knoevenagel condensation, *Angew. Chem. Int. Ed.* 60 (2021) 13614–13620, <https://doi.org/10.1002/anie.202104375>.
- [44] S. Bi, Z. Zhang, F. Meng, D. Wu, J. Chen, F. Zhang, Heteroatom-embedded approach to vinylene-linked covalent organic frameworks with isoelectronic structures for photoredox catalysis, *Angew. Chem. Int. Ed.* 134 (2022) e202111627, <https://doi.org/10.1002/ange.202111627>.
- [45] S. Wei, F. Zhang, W. Zhang, P. Qiang, K. Yu, X. Fu, D. Wu, S. Bi, F. Zhang, Semiconducting 2D triazine-cored covalent organic frameworks with unsubstituted olefin linkages, *J. Am. Chem. Soc.* 141 (2019) 14272–14279, <https://doi.org/10.1021/jacs.9b06219>.
- [46] J. Xu, Y. He, S. Bi, M. Wang, P. Yang, D. Wu, J. Wang, F. Zhang, An olefin-linked covalent organic framework as a flexible thin-film electrode for a high-performance micro-supercapacitor, *Angew. Chem. Int. Ed.* 1 (2019) 12193–12197, <https://doi.org/10.1002/ange.201905713>.
- [47] S. Bi, C. Yang, W. Zhang, J. Xu, L. Liu, D. Wu, X. Wang, Y. Han, Q. Liang, F. Zhang, Two-dimensional semiconducting covalent organic frameworks via condensation at arylmethyl carbon atoms, *Nat. Commun.* 10 (2019) 2467, <https://doi.org/10.1038/s41467-019-10504-6>.
- [48] S. Bi, P. Thiruvengadam, S. Wei, W. Zhang, F. Zhang, L. Gao, J. Xu, D. Wu, J. S. Chen, F. Zhang, Vinylene-bridged two-dimensional covalent organic frameworks via knoevenagel condensation of tricyanomesitylene, *J. Am. Chem. Soc.* 142 (2020) 11893–11900, <https://doi.org/10.1021/jacs.0c04594>.
- [49] J. Xu, C. Yang, S. Bi, W. Wang, Y. He, D. Wu, Q. Liang, X. Wang, F. Zhang, Vinylene-linked covalent organic frameworks (COFs) with symmetry-tuned polarity and photocatalytic activity, *Angew. Chem. Int. Ed.* 132 (2020) 24053–24061, <https://doi.org/10.1002/ange.202011852>.
- [50] Y.J. Li, W.R. Cui, Q.Q. Jiang, Q. Wu, R.P. Liang, Q.X. Luo, J.D. Qiu, A general design approach toward covalent organic frameworks for highly efficient electrochemiluminescence, *Nat. Commun.* 12 (2021) 4735, <https://doi.org/10.1038/s41467-021-25013-8>.
- [51] Y. Wang, W. Hao, H. Liu, R. Chen, Q. Pan, Z. Li, Y. Zhao, Facile construction of fully sp²-carbon conjugated two-dimensional covalent organic frameworks containing benzobisthiazole Units, *Nat. Commun.* 13 (2022) 100, <https://doi.org/10.1038/s41467-021-27573-1>.
- [52] K. Zhang, X. Li, L. Ma, F. Chen, Z. Chen, Y. Yuan, Y. Zhao, J. Yang, J. Liu, K. Xie, K. Loh, Fluorinated covalent organic framework-based nanofluidic interface for robust lithium–sulfur batteries, *ACS. Nano* 17 (2023) 2901–2911, <https://doi.org/10.1021/acsnano.2c11300>.
- [53] J. Xu, S. An, X. Song, Y. Cao, N. Wang, X. Qiu, Y. Zhang, J. Chen, X. Duan, J. Huang, W. Li, Y. Wang, Towards high performance Li-S batteries via sulfonate-rich COF-modified separator, *Adv. Mater.* 33 (2021) 2105178, <https://doi.org/10.1002/adma.202105178>.
- [54] Y. Cao, C. Liu, M. Wang, H. Yang, S. Liu, H. Wang, Z. Yang, F. Pan, Z. Jiang, J. Sun, Lithiation of covalent organic framework nanosheets facilitating lithium-ion transport in lithium-sulfur batteries, *Energy Storage Mater.* 29 (2020) 207–215, <https://doi.org/10.1016/j.ensm.2020.04.029>.